J. Plasma Physics (2003), *vol.* 69, *part* 4, *pp.* 277–304. © 2003 Cambridge University Press
DOI: 10.1017/S0022377803002216 Printed in the United Kingdom

Hybrid magnetohydrodynamic–kinetic model of standing shear Alfvén waves

PETER A. DAMIANO†,
R. D. SYDORA and J. C. SAMSON
Department of Physics, University of Alberta, Edmonton, Alberta, Canada T6G 2J1

(Received 13 September 2002)

Abstract. We have developed a hybrid magnetohydrodynamics (MHD) –kinetic box model valid for standing shear Alfvén waves using the cold plasma MHD equations coupled to a system of kinetic electrons. The guiding centre equations are used for the motion of the electrons and the system is closed via an expression for the field-aligned electric field in terms of the perpendicular electric field and moments of the electron distribution function. The perpendicular electric fields are derived from the ideal MHD approximation. We outline the basic model equations and method of solution. Simulations are then presented comparing the hybrid model results with a cold plasma MHD model. Landau damping is shown to heavily damp the standing shear Alfvén wave in the hybrid simulations when $v_{th} \geqslant V_A$. The damping rate is shown to be in good agreement with the theoretical rate calculated for the model parameters.

1. Introduction

Geomagnetic field line resonances and solar coronal loops are two examples of standing shear Alfvén wave (SAW) systems that are currently the topic of much study as related to auroral arc formation (Rankin et al. 1999; Streltsov and Lotko 1999) in the former case and solar coronal heating due to resonant absorption in the latter (Ionson 1978; Beliën et al. 1999). The large dimensions of these problems generally makes these systems difficult to approach using particle-in-cell (PIC) methods, but standard magnetohydrodynamics (MHD) methods cannot resolve the wave–particle interactions which are sometimes important (Rankin et al. 1999).

One alternative to full PIC simulations is the use of a hybrid code (Winske and Quest 1986). Traditional hybrid models couple kinetic ions with an electron fluid and have a long history of successful use. However, in standing SAW systems, wave–particle interactions with electrons are of fundamental importance and so another type of hybrid code is needed. The development of such a code is simplified by the fact that in standing SAW systems, the parallel current is predominantly electron current while the perpendicular current is mostly ion polarization current. This is because electrons can move very rapidly along the field lines while the ions are massive enough to cross the field lines. The parallel electron current is the plasmas

† Present address: Mathematical Institute, University of St Andrews, St Andrews, Fife KY16 9SS, UK. pdamiano@mcs.st-and.ac.uk.

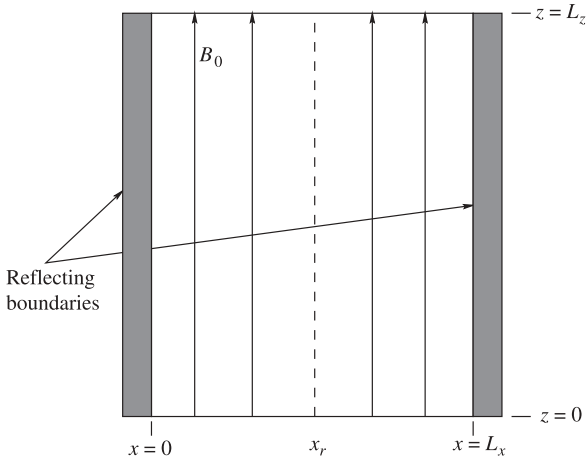

Figure 1. Two-dimensional box model.

response to the ion polarization current in a bid to maintain quasi-neutrality. Therefore, if we break up the geometry into field-aligned and perpendicular, the guiding centre equations are an excellent set to use to evolve a system of kinetic electrons and completely define the parallel current. This can be coupled to an ion fluid in a variety of ways and the system closed via an expression for the parallel electric field. The use of the guiding centre equations is justified since electron gyroradii are so much smaller than most space plasma scales. The one limiting feature of such a model is that any perpendicular scale lengths must be larger than the average ion gyroradius.

Hui and Seyler (1992) first used a model of this type to examine electron acceleration due to wave breaking of SAWs. They initialized the system by perturbing the electron density and the ion fluid was represented by an expression derived from the definition of the ion polarization current. Lyster and Leboeuf (1992) used the reduced MHD equations to represent the ions in an electrostatic model, but since standing SAWs are intrinsically electromagnetic, a more general approach is needed.

In this paper, we develop a new version of such a model, valid for low-frequency waves, where the cold plasma MHD equations are used to represent the ions. The perpendicular electric fields are obtained from the ideal MHD approximation. The system is closed via an expression of the parallel electric field in terms of the perpendicular electric field and the moments of the electron distribution function.

2. Governing equations

In this section, the basic two-dimensional (2D) model equations are introduced. For the construction of the box model as shown in Fig. 1, the field-aligned (parallel) direction is in the z-direction and the ambient magnetic field B_0 is constant. The Alfvén velocity V_A and plasma ambient plasma density ρ_0 vary in the x-direction as illustrated in Fig. 2.

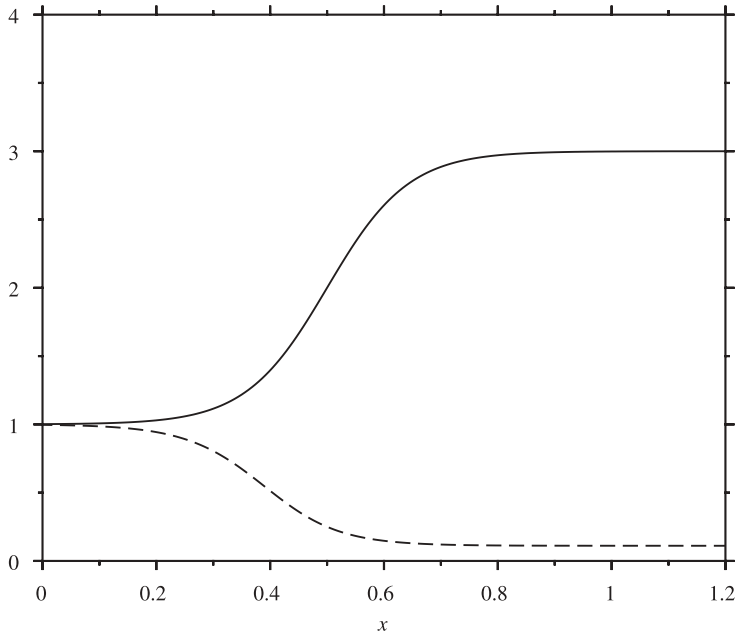

Figure 2. Graphs of V_A versus x (solid line) and ρ versus x (dashed line).

2.1. Cold plasma equations

Although the model is two dimensional, all variables are chosen to have a y dependence consistent with the choice that the cold plasma fluid velocity component u_x varies as $\sin(k_y y)$. With this choice, the individual components of the velocity $\mathbf{u}$, perturbed magnetic field $\mathbf{b}$ and electric field $\mathbf{E}$ vary as

$$\mathbf{u} = \begin{Bmatrix} u_x(x,z,t)\sin(k_y y) \\ u_y(x,z,t)\cos(k_y y) \\ 0 \end{Bmatrix}$$

$$\mathbf{b} = \begin{Bmatrix} b_x(x,z,t)\sin(k_y y) \\ b_y(x,z,t)\cos(k_y y) \\ b_z(x,z,t)\sin(k_y y) \end{Bmatrix}$$

$$\mathbf{E} = \begin{Bmatrix} E_x(x,z,t)\cos(k_y y) \\ E_y(x,z,t)\sin(k_y y) \\ E_z(x,z,t)\cos(k_y y) \end{Bmatrix}$$

and the two-dimensional cold plasma equations are denoted by

$$\frac{\partial u_x(x,z,t)}{\partial t} = \frac{B_0}{\mu_0 \rho}\left[\frac{\partial b_x(x,z,t)}{\partial z} - \frac{\partial b_z(x,z,t)}{\partial x}\right]$$

$$\frac{\partial u_y(x,z,t)}{\partial t} = \frac{B_0}{\mu_0 \rho}\left[\frac{\partial b_y(x,z,t)}{\partial z} - k_y b_z(x,z,t)\right]$$

$$\frac{\partial b_x(x,z,t)}{\partial t} = \frac{\partial E_y(x,z,t)}{\partial z} + k_y E_z(x,z,t)$$

$$\frac{\partial b_y(x,z,t)}{\partial t} = \frac{\partial E_z(x,z,t)}{\partial x} - \frac{\partial E_x(x,z,t)}{\partial z}$$

$$\frac{\partial b_z(x,z,t)}{\partial t} = -\left[k_y E_x(x,z,t) + \frac{\partial E_y(x,z,t)}{\partial x}\right].$$

The perpendicular electric field values are determined via the ideal MHD approximation, $\mathbf{E}_\perp = -\mathbf{u} \times \mathbf{B}_0$ while the parallel electric field, E_z, is determined from an algorithm described in Sec. 2.3.

2.2. Guiding centre equations

Neglecting all the drifts, except for $\mathbf{E} \times \mathbf{B}$, along with the field definitions already stated, allows the guiding centre equations for electron motion (Parks 1991) to be written simply as

$$\frac{\partial v_z}{\partial t} = -\frac{e}{m_e} E_z(r_{gx}, r_{gz}, t)\cos(k_y y) \tag{2.1}$$

$$\frac{\partial r_{gz}}{\partial t} = v_z \tag{2.2}$$

$$\frac{\partial r_{gx}}{\partial t} = \frac{1}{B_0}[v_z b_x(r_{gx}, r_{gz}, t) + E_y(r_{gx}, r_{gz}, t)]\sin(k_y y), \tag{2.3}$$

where r_{gx} and r_{gz} are, respectively, the x and z components of the electron guiding centre position, $\mathbf{r}_g$, and v_z is the field-aligned component of the guiding centre velocity. It should be noted that the mirror term is neglected because of the straight magnetic field configuration, but will be included in a future model involving curvature. The use of the guiding centre equations is justified since for homogeneous auroral arcs, the typical minimum scale lengths are on the order of a kilometre which is well above the typical electron gyroradius.

2.3. Parallel electric field

The combined system of the cold plasma equations and the guiding centre equations for the electrons needs to be closed via the parallel electric field E_z. This is derived as follows. Taking the partial time derivative of Ampère's law and combining with Faraday's law yields

$$-\nabla \times [\nabla \times \mathbf{E}(\mathbf{r})] = \mu_0 \frac{\partial \mathbf{j}(\mathbf{r})}{\partial t}. \tag{2.4}$$

Using the vector identity $\nabla \times (\nabla \times \mathbf{E}) = \nabla(\nabla \cdot \mathbf{E}) - \nabla^2 \mathbf{E}$, this becomes

$$\nabla^2 \mathbf{E}(\mathbf{r}) - \nabla[\nabla \cdot \mathbf{E}(\mathbf{r})] = \mu_0 \frac{\partial \mathbf{j}(\mathbf{r})}{\partial t} \tag{2.5}$$

and taking only the z component we are left with

$$\nabla^2 E_z(\mathbf{r}) - \frac{\partial[\nabla \cdot \mathbf{E}(\mathbf{r})]}{\partial z} = \mu_0 \frac{\partial j_z(\mathbf{r})}{\partial t}. \tag{2.6}$$

For the SAW system, the parallel current is entirely due to the electrons and so j_z can be replaced by the electron current, $j_e(\mathbf{r}) = -e\sum_i v_i S(\mathbf{r}, \mathbf{r}_i)$, where $v = v_z$

and S is a particle shape function related to the discretization of charge (Birdsall and Langdon 1991). Substituting this in for j_z and expanding the time derivative yields

$$\nabla^2 E_z(\mathbf{r}) - \frac{\partial[\nabla\cdot\mathbf{E}(\mathbf{r})]}{\partial z} = -e\mu_0\left[\frac{\partial v_i}{\partial t}S(\mathbf{r},\mathbf{r}_i) + v_i\frac{\partial S(\mathbf{r},\mathbf{r}_i)}{\partial t}\right]. \tag{2.7}$$

The notation j_e has been introduced simply to stress the fact that the parallel current is coming from the kinetic electrons and not from the solution of Ampère's law. The notation j_z will be used from now on to signify the solution of Ampère's law. When the hybrid model is working properly, these two variables should have the same value within a small numerical error. Now, with the use of the electron momentum equation $\frac{\partial v_i(\mathbf{r})}{\partial t} = -\frac{e}{m_e}E_z(\mathbf{r})$, the last expression becomes

$$\nabla^2 E_z(\mathbf{r}) - \frac{\partial[\nabla\cdot\mathbf{E}(\mathbf{r})]}{\partial z} = -e\mu_0\sum_i\left[v_i\frac{\partial S(\mathbf{r},\mathbf{r}_i)}{\partial t} - \frac{e}{m_e}E_z(\mathbf{r}_i)S(\mathbf{r},\mathbf{r}_i)\right] \tag{2.8}$$

and using the continuity equation

$$\frac{dn}{dt} = \sum_i\frac{dS(\mathbf{r},\mathbf{r}_i)}{dt} = \sum_i\left[\frac{\partial S(\mathbf{r},\mathbf{r}_i)}{\partial t} + v_i\frac{\partial S(\mathbf{r},\mathbf{r}_i)}{\partial z}\right] = 0 \tag{2.9}$$

the partial time derivative of the particle shape function can be replaced with the advection term resulting with

$$\nabla^2 E_z(\mathbf{r}) - \frac{\partial[\nabla\cdot\mathbf{E}(\mathbf{r})]}{\partial z} = \frac{\mu_0 e^2}{m_e}\sum_i E_z(\mathbf{r}_i)S(\mathbf{r},\mathbf{r}_i) + \mu_0 e\sum_i v_i^2\frac{\partial S(\mathbf{r},\mathbf{r}_i)}{\partial z}. \tag{2.10}$$

Assuming $E_z(\mathbf{r}_i) \approx E_z(\mathbf{r})$, and since v and z are independent variables we then have

$$\nabla^2 E_z(\mathbf{r}) - \frac{\partial[\nabla\cdot\mathbf{E}(\mathbf{r})]}{\partial z} = \frac{\mu_0 e^2}{m_e}E_z(\mathbf{r})n_e(\mathbf{r}) + \mu_0 e\frac{\partial}{\partial z}\sum v_i^2 S(\mathbf{r},\mathbf{r}_i), \tag{2.11}$$

where $n_e(\mathbf{r}) = \sum_i S(\mathbf{r},\mathbf{r}_i)$. Rearranging, and using the definition for the electron inertial length, we have

$$\nabla^2 E_z(\mathbf{r}) - \frac{1}{\lambda_e^2(\mathbf{r})}E_z(\mathbf{r}) = \frac{\partial(\nabla\cdot\mathbf{E})}{\partial z} + \mu_0 e\frac{\partial}{\partial z}\sum v_i^2 S(\mathbf{r},\mathbf{r}_i). \tag{2.12}$$

Now for the SAW system, the parallel wavenumber is much smaller than the perpendicular values. The parallel electric field is also much smaller than E_x and E_y allowing the equation to be further simplified

$$\frac{\partial^2 E_z(\mathbf{r})}{\partial x^2} - \frac{1}{\lambda_e^2(\mathbf{r})}E_z(\mathbf{r}) = \frac{\partial(\nabla\cdot\mathbf{E}_\perp)}{\partial z} + \mu_0 e\frac{\partial}{\partial z}\sum v_i^2 S(\mathbf{r},\mathbf{r}_i). \tag{2.13}$$

This derivation is similar to the approach used by Busnardo-Neto et al. (1977) and Okuda et al. (1979) for their work on magnetostatic particle codes. The expression is the same as used by Hui and Seyler (1992) for their hybrid model, although it was derived slightly differently there by utilizing the generalized Ohm's law.

If the second term on the right-hand side is neglected, this equation along with the two-dimensional cold plasma equations are completely self-consistent and the fields can be used as input for the guiding centre equations for test-particle simulations. However, although the second term on the right-hand side incorporates the effects of electron pressure on electric field generation, the equation as is, is not sufficient for a self-consistent hybrid code. There needs to be a 'correction field'

for the charge separation induced between the fluid ions and kinetic electrons. This expression is determined as follows. Adding the continuity equations for the electrons and ions

$$\frac{\partial n_i}{\partial t} + \nabla \cdot (n_i \mathbf{v}_i) = 0 \tag{2.14}$$

$$\frac{\partial n_e}{\partial t} + \nabla \cdot (n_e \mathbf{v}_e) = 0 \tag{2.15}$$

yields

$$\frac{\partial (n_i - n_e)}{\partial t} + \nabla \cdot [(n_i v_i - n_e v_e)] = 0. \tag{2.16}$$

Using Poisson's equation

$$\nabla \cdot E = \frac{e}{\epsilon_0}(n_i v_i - n_e v_e) \tag{2.17}$$

and the definition of current density

$$\mathbf{j} = e(n_i \mathbf{v}_i - n_e \mathbf{v}_e) \tag{2.18}$$

yields the following relationship between the divergence of current and the divergence of electric field:

$$\epsilon_0 \frac{\partial}{\partial t}(\nabla \cdot \mathbf{E}_C) = -\nabla \cdot \mathbf{j}. \tag{2.19}$$

where the notation E_C has been introduced to distinguish this field from the field calculated via the ideal MHD approximation $E_\perp = -\mathbf{u} \times \mathbf{B}_0$. The coupling for the correction field comes via the use of the electron current density in the divergence of the current density, such that

$$\nabla \cdot \mathbf{j} = \frac{\partial j_x}{\partial x} + k_y j_y + \frac{\partial j_e}{\partial z} \tag{2.20}$$

where j_x and j_y come from the fluid fields. In the MHD limit $\nabla \cdot \mathbf{J} = 0$ since $\nabla \cdot (\nabla \times \mathbf{b}) = 0$ and so there is no correction field.

It should be noted that this closure is somewhat different from that used by Hui and Seyler (1992) in their hybrid model. They coupled in the electron current density moment via an expression derived from the definition of ion polarization current.

3. Numerical algorithm

3.1. Spatial and temporal discretization

The fluid equations are solved using a second-order predictor–corrector-type method. The first-order differential equation $dy/dt = F$ is finite-differenced in time as follows:

$$y_p^{t+\Delta t} = y^{t-\Delta t} + 2\Delta t F(y^t) \tag{3.1}$$

$$y^{t+\Delta t} = y^t + \frac{\Delta t}{2}\left[F(y^t) + F\left(y_p^{t+\Delta t}\right)\right], \tag{3.2}$$

where the subscript 'p' denotes the predicted value. With this scheme, it is necessary to keep track of the all values at three points in time, but the algorithm is very stable for long integration times.

The first-order derivatives in both the x- and z-directions are evaluated using a four-point formula which for a derivative with respect to x is given by

$$\frac{\partial f}{\partial x} \approx \frac{-f_{j-2} + 8f_{j-1} - 8f_{j+1} + f_{j+2}}{12\Delta x}, \tag{3.3}$$

where Δx is the distance between adjacent grid points in the x-direction.

3.2. Normalization

In order to normalize the fluid equations, the following set of variables are introduced

$$\mathbf{r}' = \frac{\mathbf{r}}{L_N}; \quad t' = \frac{t}{t_N}; \quad \mathbf{B}' = \frac{\mathbf{B}}{B_0}; \quad \mathbf{V}' = \frac{\mathbf{V}}{V_N}; \quad \rho' = \frac{\rho}{\rho_O}; \quad \mathbf{j}' = \frac{\mathbf{j}}{j_N}; \quad \mathbf{E}' = \frac{\mathbf{E}}{E_N} \tag{3.4}$$

where $L_N = R_E$, $\rho_N = \rho(x = 0)$, $V_N = \sqrt{B_0/(\mu_0\rho_N)}$, $t_N = L_N/V_N$, $j_N = B_0/(\mu_0 L_N)$ and $E_n = V_N B_0$. The primes will be left out though for simplicity of notation.

3.3. Particle loading and grid interpolation

The fluid equations are solved on a two-dimensional grid where the number of points in each direction can be specified independently. At $t = 0$, the ambient Alfvén velocity and corresponding density are specified at the grid points. They vary as a function of x but are constant in the z-direction. The electrons are loaded to follow this density profile. This 2D loading of electrons is accomplished by initially specifying the number of initial positions in the x- and the z-direction given by n_{p_x} and n_{p_z}, respectively, where $n_p = n_{p_x} n_{p_z}$ is the total number of particles. The n_{x_p} positions are then assigned using a cumulative probability approach where the radial fluid density function is the probability distribution function (Gould and Tobochnik 1996). With these x positions assigned, n_{z_p} electrons are then placed at each of these positions equally spaced in z. The velocities are assigned to the electrons using the cumulative probability approach as well, but with a Maxwellian function given by

$$f(v_z) = \frac{n}{\sqrt{\pi} v_{th}} \exp\left(-\frac{v_z^2}{v_{th}^2}\right) \tag{3.5}$$

as the probability distribution function where $v_{th} = \sqrt{2k_B T/m_e}$.

The fluid equations are solved at the grid points, but the electrons are free to move anywhere in the two-dimensional space. The field values are interpolated to the electron position and the moments of the electron distribution are then interpolated to the grid using a biquadratic spline approach (Birdsall and Langdon 1991).

3.4. Scaling of electron number density

The number of kinetic electrons is scaled to represent the number implied by the plasma density via a factor calculated from the ratio of the fluid number density $n_f(\mathbf{r})$ (where $\mathbf{r} = (x, z)$) and the first moment of the electron distribution function at $t = 0$ (t_0), $\sum_i S(\mathbf{r}, \mathbf{r}_i, t_0)$. The scaled electron current density is then

$$j_e(x, y, z, k_y, t) = j_e(x, z, t)\cos(k_y y) = -e\frac{n_f(x, z)}{\sum_i S(\mathbf{r}, \mathbf{r}_i, t_0)} \sum_i v_i S(\mathbf{r}, \mathbf{r}_i, t). \tag{3.6}$$

Therefore, the electron current density that is input into the fluid model is given by

$$j_e(x,z,t) = \frac{-e}{\cos(k_y y)} \frac{n_f(x,z)}{\sum_i S(\mathbf{r},\mathbf{r}_i,t_0)} \sum_i v_i S(\mathbf{r},\mathbf{r}_i,t). \tag{3.7}$$

Since the kinetic electron density profile scales as the fluid density profile, this ratio is constant and each kinetic electron is representative of an equal number of 'real electrons' everywhere in the simulation space.

The second moment term in the equation for the parallel electric field (2.13) is scaled in the same way and using the phase choices discussed earlier. The final form of this equation is

$$\begin{aligned} &\frac{\partial^2 E_z(x,z,t)}{\partial x^2} - \frac{1}{\lambda_e^2(\mathbf{r})} E_z(x,z,t) \\ &\quad = \frac{\partial[\nabla\cdot\mathbf{E}_\perp(x,z,t)]}{\partial z} + \mu_0 e \frac{n_f(x,z)}{\sum_i S(\mathbf{r},\mathbf{r}_i,t_0)\cos(k_y y)} \frac{\partial}{\partial z} \sum_i v_i^2 S(\mathbf{r},\mathbf{r}_i,t). \end{aligned} \tag{3.8}$$

This can be solved quite readily for E_z using a three-point finite-difference representation of $\partial^2/\partial x^2$ and a tridiagonal matrix solver.

3.5. Test particle and coupled modes

The model is designed to be used as either a test-particle code or as a full hybrid model when the coupling is turned on. For the test-particle model, the pressure term in (3.8) is neglected and the correction field E_C is not determined. For the hybrid model, $\nabla\cdot\mathbf{E}_C$ is determined with a modified Euler scheme such that

$$\nabla\cdot\mathbf{E}_C^{n+1} = \nabla\cdot\mathbf{E}_C^{n} - dt\frac{1}{2\epsilon_0}[(\nabla\cdot\mathbf{j})_c + (\nabla\cdot\mathbf{j})_p],$$

where $(\nabla\cdot\mathbf{j})_c$ and $(\nabla\cdot\mathbf{j})_p$ are the divergences of current determined at the predictor and corrector steps, respectively. This divergence is then used at the end of the corrector step to determine E_z for the next time step as follows:

$$\begin{aligned} &\nabla^2 E_z^{n+1}(x,z) - \frac{1}{\lambda_e^2(\mathbf{r})} E_z^{n+1}(x,z) \\ &\quad = \frac{\partial\big(\nabla\cdot\mathbf{E}_\perp^{n+1} + \nabla\cdot\mathbf{E}_C^{n+1}\big)}{\partial z} + \mu_0 e \frac{n_f(x,z)}{\sum_i S(\mathbf{r},\mathbf{r}_i,t_0)\cos(k_y y)} \frac{\partial}{\partial z} \sum v_i^2 S(\mathbf{r},\mathbf{r}_i). \end{aligned}$$

3.6. Filtering

In order to reduce the statistical noise in the model we apply a two-dimensional filter (Birdsall and Langdon 1991) to the three moments of the electron distribution function as well as the parallel electric field. This is done at both predictor and corrector steps. The lowest-order filter is used, which in one dimension is given by

$$F_i' = \tfrac{1}{4}F_{i-1} + \tfrac{1}{2}F_i + \tfrac{1}{4}F_{i+1}. \tag{3.9}$$

This is applied first in the x-direction and then in the z-direction. This method has worked very effectively except with regards to the parallel electric field as will be commented on later. This latter point aside, filtered and unfiltered runs at low temperatures yield quantitatively similar results.

3.7. Boundary conditions

At the z boundaries, we use periodic boundary conditions. Electrons passing through one boundary, are reintroduced at the other boundary with the same velocity. At the x boundaries, perfectly reflecting boundary conditions are used. This translates into boundary conditions on the five fluid variables of $u_x = b_x = 0$ and $\partial u_y/\partial x = \partial b_y/\partial x = \partial b_z/\partial x = 0$. In terms of the electrons, they are initially positioned so that the x boundaries are half way in between the first two grid points at $x = 0$ and the last two grid points at the $x = L_x$ end. As will become evident, the x drift of the electrons is negligible and so it is rare for them to interact with the x boundary. If the boundary is crossed, they are simply repositioned slightly inwards from the boundary at the same position in z. This solution is only first order, but it is stable for the models we are considering.

4. Numerical results

4.1. Model parameters

Although, the equations are solved in non-dimensional form, all values for the initial variables were chosen to approximately correspond to conditions in the Earth's dayside equatorial magnetosphere before being made non-dimensional. The ambient magnetic field B_0 and density ρ_N were chosen to be 10 nT and $10^5 m_p\,\mathrm{m}^{-3}$, respectively, where m_p is the proton mass in kg. This yields a value of $v_N = 6.9 \times 10^5\,\mathrm{m\,s^{-1}}$. The non-dimensional Alfvén velocity profile is then specified with the function

$$v_A = \tanh(\alpha x + \phi) + \beta \tag{4.1}$$

where $\alpha = 7$, $\beta = 2$ and $\phi = -0.5$ and because of the constant ambient magnetic field, the non-dimensional density is simply given by

$$\rho = \frac{1}{v_A^2}. \tag{4.2}$$

Both functions are displayed in Fig. 2. The corresponding inertial Alfvén length profile is calculated in MKS units and then normalized by the characteristic length, $L_N = 1R_E$. The profile is displayed in Fig. 3.

The radial dimension of the simulation box is taken to be $L_x = 1.2R_E$ while the parallel length is chosen to be $L_z = 18R_E$. This is roughly the length of a dipolar magnetic field which cuts through the equatorial plane at a distance of $8R_E$ from the Earth. As field line resonances associated with auroral arc formation most typically occur along field lines which are 8–12R_E from the Earth in the equatorial plane (Fenrich 1997), the dimensions of the simulation box roughly correspond to the proper scales.

For all the simulations presented here, we used a grid of 200 points in the x-direction and 25 points in the z-direction. Although the code is able to simulate the full mode conversion process, we initialized only a standing SAW with a Gaussian profile for u_y as a function of x (see Fig. 4) and a $\sin(k_z z)$ profile was chosen for the z-direction, i.e.

$$u_y(t=0) = A \exp\left[\frac{-(x-x_r)^2}{2w^2}\right] \sin(k_z z) \tag{4.3}$$

where $w = 0.05$ and $A = 0.05$ corresponds to a maximum shear velocity of $34.5\,\mathrm{km\,s^{-1}}$ and the parallel wavenumber, $k_z = 2\pi/L_z$, where $L_z = 18$ in

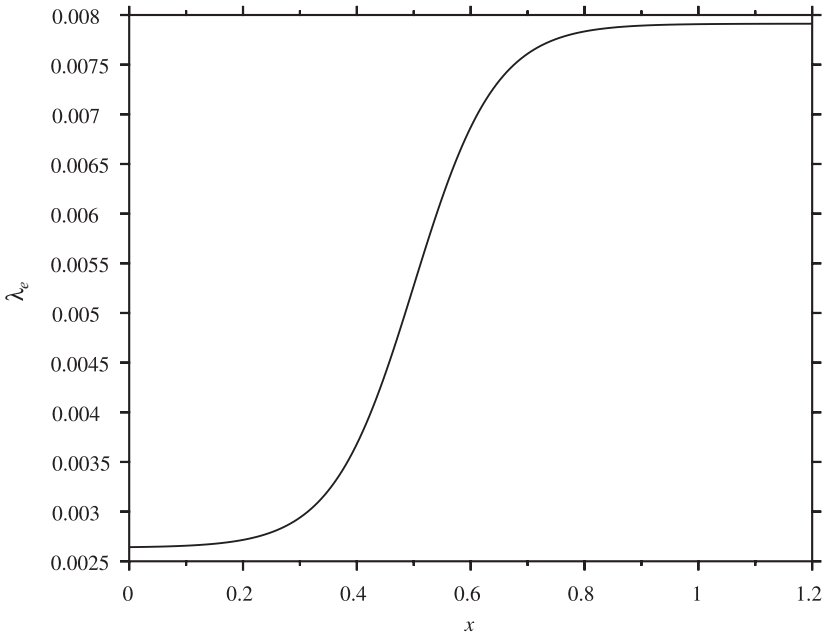

Figure 3. Graph of electron inertial length λ_e versus x.

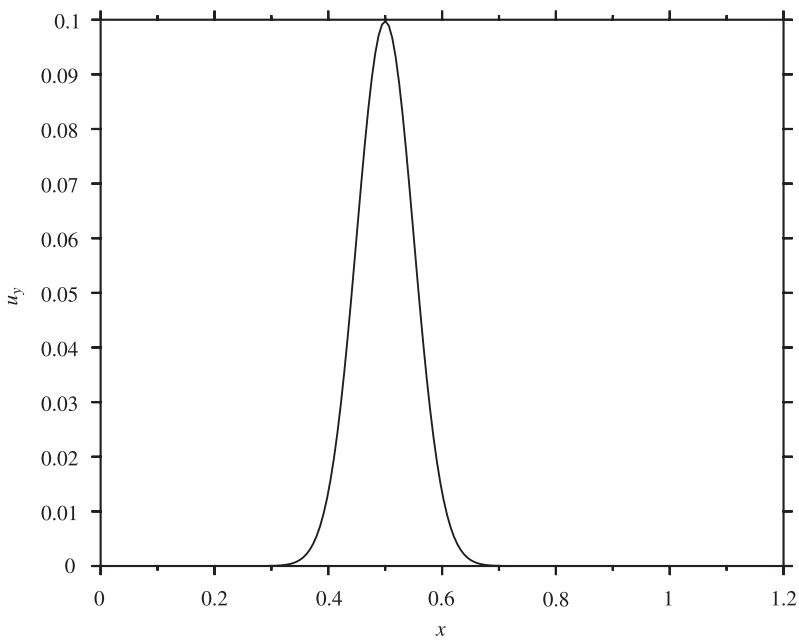

Figure 4. Graph of initial shear Alfvén velocity profile in the x-direction.

non-dimensional units. The position of the resonance is chosen to be $x_r = 0.5$. For these parameters, the SAW dispersion relation $\omega^2 = k_z^2 V_A^2$ yields a frequency and period for the resonance that are calculated to be $\omega = 0.0755\ \mathrm{s}^{-1}$ and $T_A = 83.2$ s,

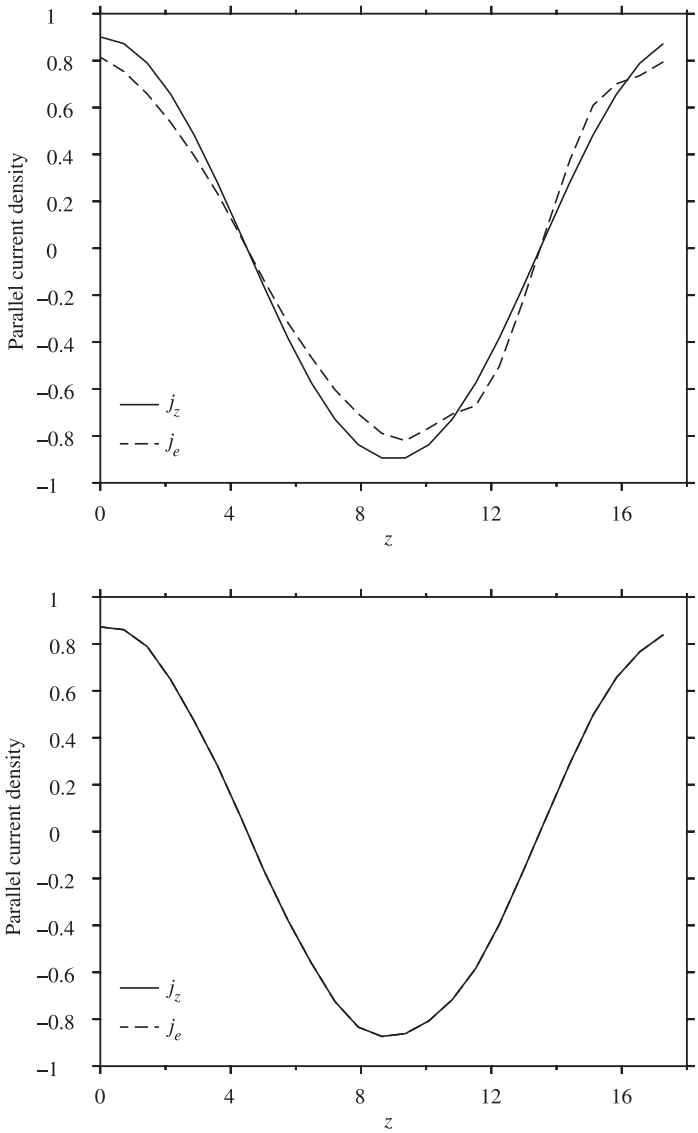

Figure 5. Comparison of kinetic electron current j_e and the Ampère's law current j_z from the test-particle model (top) and the hybrid model (bottom) at $t = 2T_A$. Slice at $x = 0.597$.

respectively. For the simulations presented here, 70 000 time steps were used for a time of $10T_A$. Although not displayed here, the numerical period of oscillation of the shear velocity at the resonance position is found to be in excellent agreement with the value calculated from the dispersion relation.

For the electrons we need to select a slice in y. In order not to have much leaking of energy from the shear mode we chose a small value for $k_y = 0.42$ and correspondingly chose y so that $k_y y = \pi/4$. As this is a 2D model, all electrons have the same position in y.

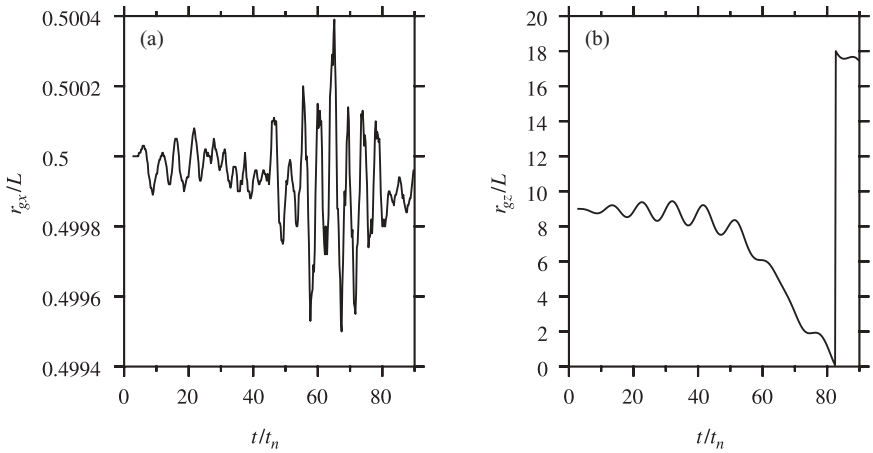

Figure 6. (a) The radial motion of an electron guiding centre in the standing SAW system. (b) The field-aligned motion.

4.2. Comparison of test-particle and hybrid model results

Test-particle calculations are a common first starting point for many studies of wave–particle interactions and so it is always good to compare test-particle results with more self-consistent calculations to see how far the approximation is justified. As indicated earlier, the hybrid code can be run in test-particle mode and a comparison was made between the uncoupled and coupled codes in the limit of an initial electron δ-function distribution. Figure 5 displays the results of both calculations with the test-particle and hybrid results in the top and bottom panels, respectively, at $t = 2T_A$. In the test-particle case, the kinetic electron current j_e already starts to diverge strongly from the solution of Ampère's law (j_z) while in the hybrid case, the two quantities are virtually identical. Therefore, with no feedback of the electrons on the fluid, it only takes two to three oscillation periods before the test-particle approach starts to become invalid.

4.3. Parallel and perpendicular electron motion

Figure 6 illustrates the radial and field-aligned motion of the guiding centre of an electron started at $(x, z) = (0.5, 9)$ with an initial velocity $v_{gz} = 0$. As is evident, the x motion of the electron is negligible relative to the field-aligned motion which is consistent with the current picture within a field line resonance as outlined in Sec. 2. The shift of the electron position at $t \approx 85$ is the electron passing through one boundary and re-entering at the other (and vice versa).

4.4. Comparison of hybrid model simulations for different initial distributions

As is evident from Fig. 2, the Alfvén velocity at the resonance position is 2 in non-dimensional units and so the phase velocity of the standing SAW is $\omega/k_z = \pm 2 = v_{ph}$. For the purposes of this section, we simply denote this local Alfvén speed as V_A and use it to define three regions of consideration, $v_{th} \ll V_A$, $v_{th} \approx V_A$ and $v_{th} > V_A$, where v_{th} is the average thermal velocity of the distribution function. To accomplish this, we present simulations with four different initial distribution functions, a δ-function distribution ($v_{th} = 0$) and three Maxwellian distributions ($v_{th} = 0.71$, 1.41, 4.24). All hybrid model simulations used 10^6 particles ($n_{p_x} = 1000$, $n_{z_p} = 1000$)

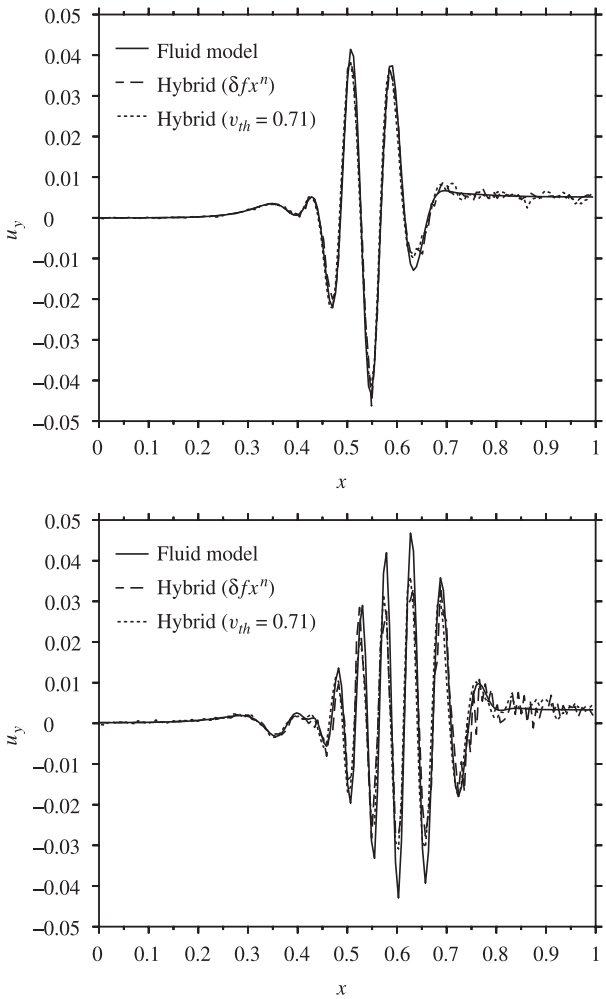

Figure 7. Top: comparison of azimuthal velocity at $t = 4T_A$ from the fluid model (solid line) and the hybrid model for the initial δ-function–electron distribution (dashed line) and $v_{th} = 0.71$ initial electron distribution function (dotted line). Slice at $z = 3.6$. Bottom: same at $t = 8T_A$.

except in the $v_{th} = 4.24$ case where 2×10^6 particles ($n_{p_x} = 1000$, $n_{z_p} = 2000$) were used. The illustrated distribution functions are average distribution functions compiled using electrons close to the resonance, $(0.5 \leqslant x \leqslant 0.65)$ and anywhere in the z plane. 100 velocity bins are used in the compilation.

For the case of the cold plasma limit, Fig. 7 illustrates the azimuthal velocity at $t = 4T_A$ and $8T_A$ for the fluid model and the hybrid model using the initial δ-function distribution and the $v_{th} = 0.71$ distribution. As would be expected, the hybrid description and the cold plasma MHD fluid description diverge little. The formation of an inertial SAW propagating to the right (the direction if increasing Alfvén wave speed) is evident.

The case of $v_{th} \approx V_A$ is illustrated in Fig. 8 where the azimuthal velocity for the hybrid model using $v_{th} = 1.41$ for $t = 4T_A$ and $7T_A$ is displayed along with the

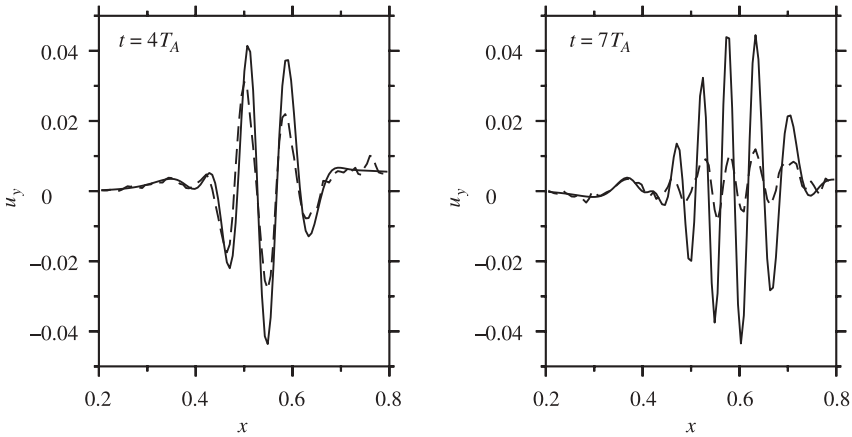

Figure 8. Comparison of azimuthal velocity from the fluid model (solid line) and the hybrid model with $v_{th} = 1.41$ (dashed line). Slice at $z = 3.6$.

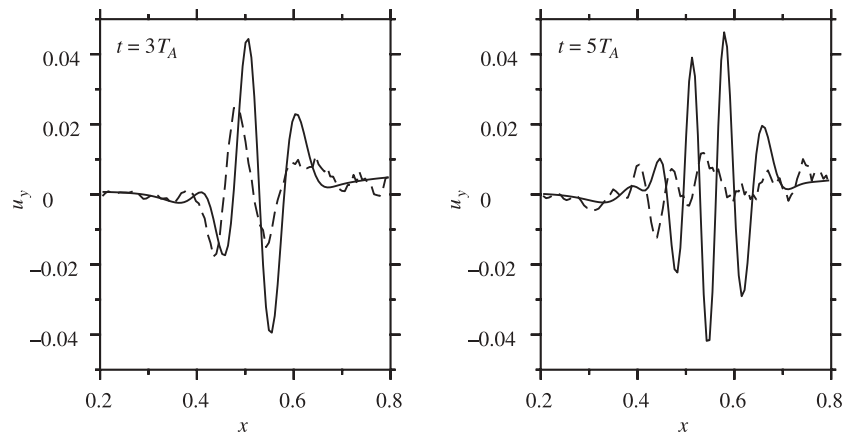

Figure 9. Comparison of the azimuthal velocity from the fluid model (solid line) and the hybrid model (dashed line) with $v_{th} = 4.24$. Slice at $z = 3.6$.

MHD results. The gradual Landau damping of the SAW as a function of time is clearly evident. The numerical damping rate measured from this calculation will be compared with the theoretical value determined from the dispersion relation in a later subsection.

The final example of $v_{th} > V_A$ is illustrated in Fig. 9 where the evolution of the azimuthal velocity at $t = 3T_A$ and $5T_A$ are shown. The resonance in the hybrid model is seen to maintain its position while it propagates as an inertial wave pulse in the cold plasma MHD limit. As the temperature increases, the system approaches the kinetic Alfvén wave regime and a close examination indicates a slight propagation in the direction of decreasing Alfvén wave speed. The wave is strongly damped and has negligible amplitude by $t = 6T_A$.

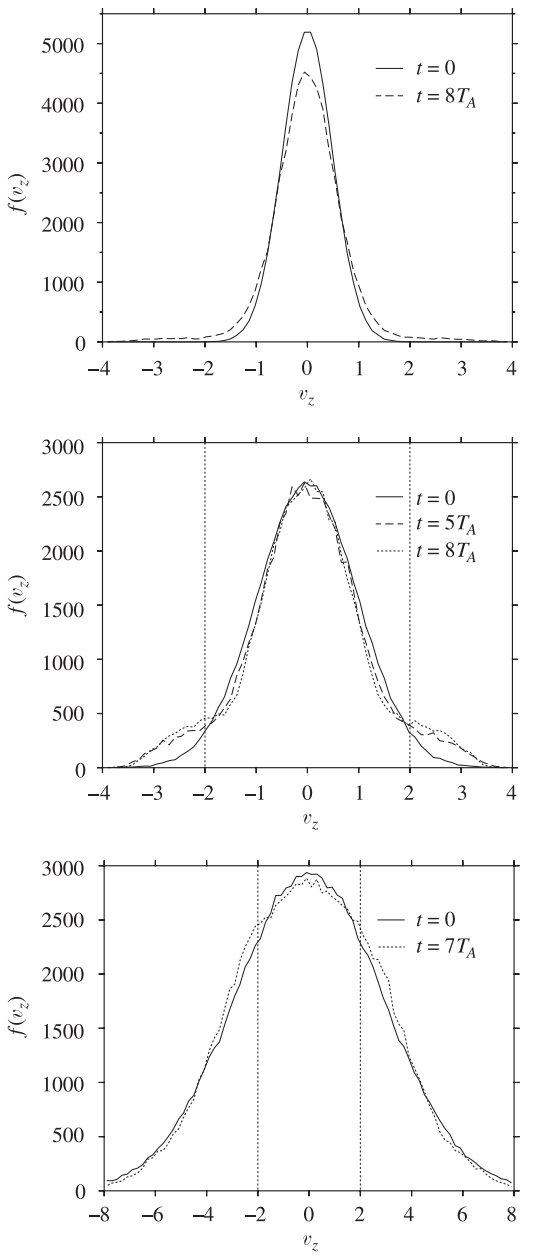

Figure 10. Distribution function evolution. Top: case of $v_{th} = 0.71$. Middle: case of $v_{th} = 1.41$. Bottom: case of $v_{th} = 4.24$.

The evolution of the corresponding electron distribution functions are illustrated in Fig. 10. The top panel illustrates the $v_{th} = 0.71$ distribution case and it is evident that the distribution function is heated a little during the length of the simulation, but only changes marginally. In the middle panel $v_{th} = 1.41$ case is presented. The Maxwellian is being modified at $v_z = \pm 2$ which, as mentioned previously, is the classic plateauing due to Landau trapping effects. The warmest case, $v_{th} = 4.24$

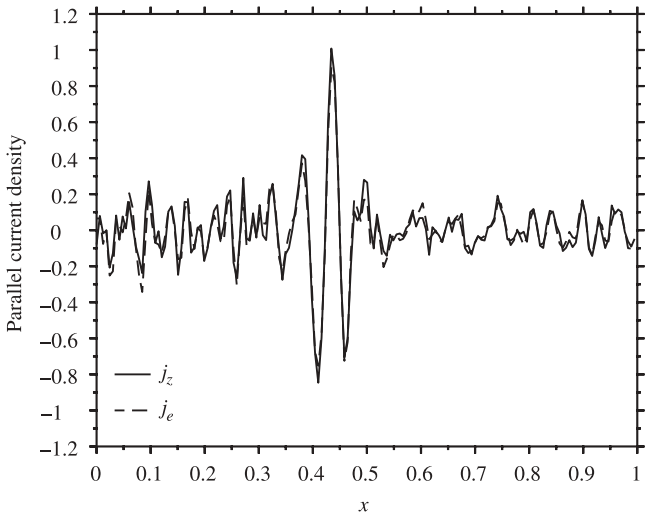

Figure 11. Comparison of kinetic parallel electron current j_e (dashed line) and the solution of Ampère's law, j_z, at $t = 5T_A$ for $v_{th} = 4.24$. Slice at $z = 7.92$.

is highlighted in the bottom panel. The distribution function is not as strongly modified as in the $v_{th} = 1.41$ case, but there is evidence of some trapping around $v_z \approx v_{ph}$. The damping is actually stronger, as is evident from Fig. 9, because the slope of the distribution function at the resonance position is steeper than for $v_{th} = 1.41$. The lack of a strong modification of the distribution function is probably due to the larger number of electrons around the resonance position than in the previous case.

In order to confirm that Ampère's law and the kinetic electron current still agree in the case of warmer distribution function, Fig. 11 compares j_z and j_e for $v_{th} = 4.24$. It is clear, that even with the relatively large amount of noise, the two quantities stay very well synchronized with each other. Therefore, the numerical noise does not introduce any inconsistencies in the operation of the model.

4.5. Effects of particle number and density fluctuations

An important consideration in any statistical model is how the number of simulation electrons affects the results. It is necessary to have a sufficient number to adequately represent the system as well as to keep noise issues to a minimum. However, as indicated previously, the number of simulation electrons are scaled to a realistic value and so after a point, the general results should be insensitive to the simulation electron number. In order to test this, the $v_{th} = 1.41$ simulation was redone with 2×10^6 simulation electrons. The current moment results in both cases (along with the MHD results) are illustrated in Fig. 12. As is evident, there is little quantitatively significant difference until well into the run and the evolution of the system is the same in both cases. Therefore, the results of the hybrid code are robust for current parameters with $n_p \approx 1 \times 10^6$ or more. A few hundred thousand particles work as well, but the results are noisier and so the choice of 10^6 particles is a good compromise. It should be stressed that the choice of an adequate number of

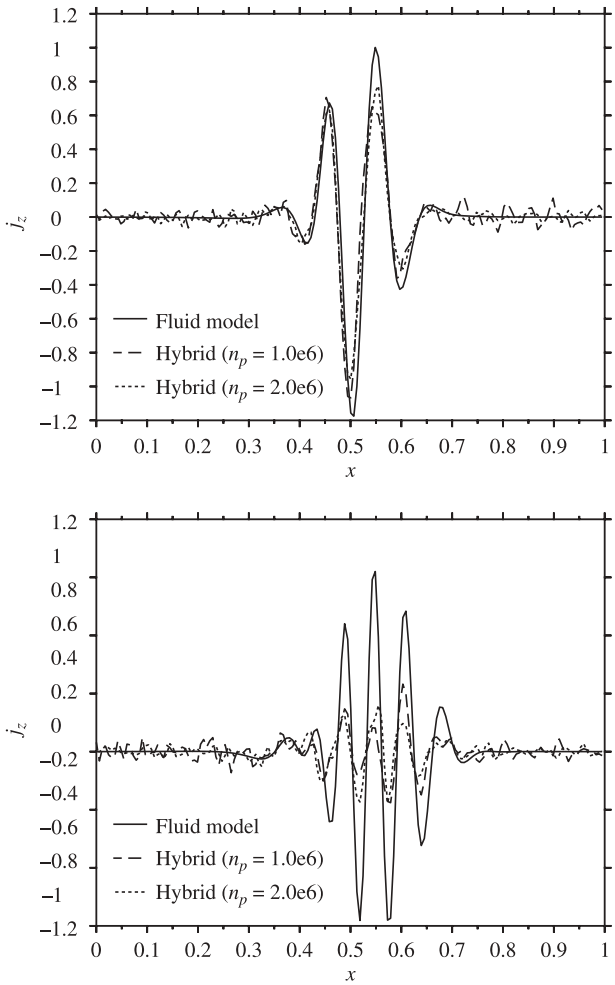

Figure 12. Top: comparison of the azimuthal velocity in the fluid model (solid line) and the hybrid model using the $v_{th} = 1.41$ initial electron distribution function with $n_p = 1 \times 10^6$ (dashed line) and $n_p = 2 \times 10^6$ (dotted line) at $t = 3T_A$. Bottom: same at $t = 7T_A$. Slice at $z = 7.92$.

particles is dependent on the initial parameters and warmer distributions require more simulation electrons.

As was mentioned earlier, the electron density distribution has the same profile as the specified fluid density. This is evident in the top panel of Fig. 13 which illustrates the unscaled electron number density at $t = 3T_A$ for hybrid model using 10^6 particles. Superimposed on the ambient density is the perturbation due to the standing SAW. The bottom panel of the same figure illustrates slices of n_e along $z = 3.6$ at the same time for both the 10^6 and 2×10^6 particle simulations. The result for the former case has been multiplied by two and lies very close to the result for the latter case. This illustrates that the ratio of the fluctuation relative to the ambient background is relatively independent of the number of simulation

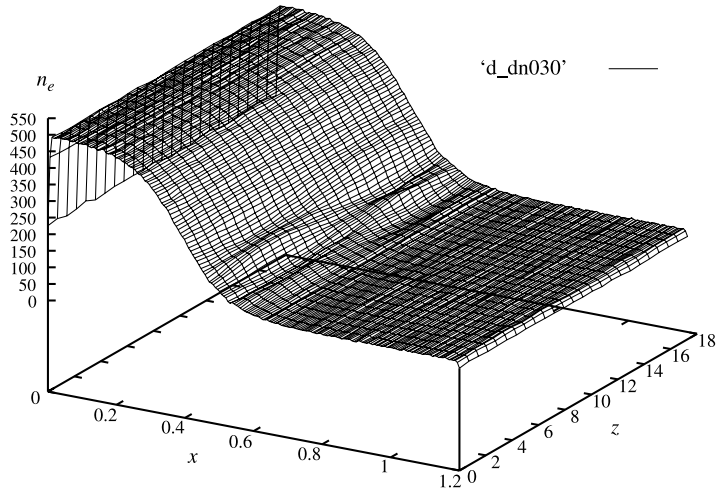

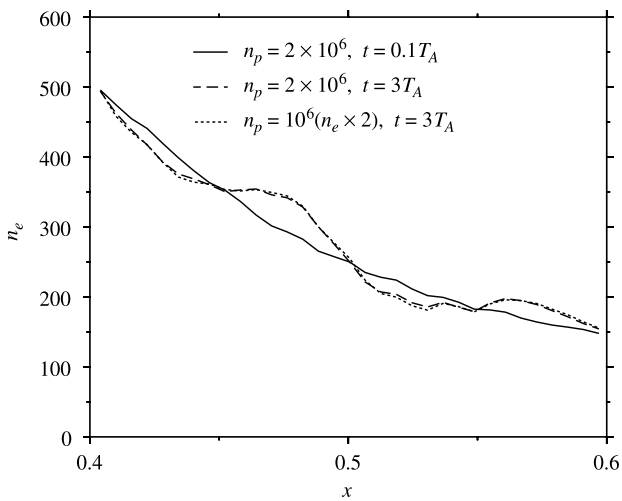

Figure 13. Top: unscaled electron number density from the hybrid model with $v_{th} = 1.41$ and $n_p = 1 \times 10^6$ at $t = 3T_A$. Bottom: slices of the unscaled electron number density at $z = 3.6$ for $t = 3T_A$ with $n_p = 1 \times 10^6$ (dashed line) and $n_p = 2 \times 10^6$ (dotted line). The ambient density profile is indicated by the solid line for $t = 0.1T_A$.

electrons. The magnitude of the background density is evident from the slice at $t = 0.1T_A$.

4.6. Parallel electric field

As alluded to earlier, the parallel electric field is typically too noisy to be visible, even with the smoothing algorithm used. However, the field can be seen with the application of a post-simulation spectral filter using the hyper-Gaussian function ($e^{-(i/n)^{20}}$, where i is the spectral mode and n is a parameter to be specified) to filter out higher-order spectral modes. The filtering, in each direction, is accomplished by

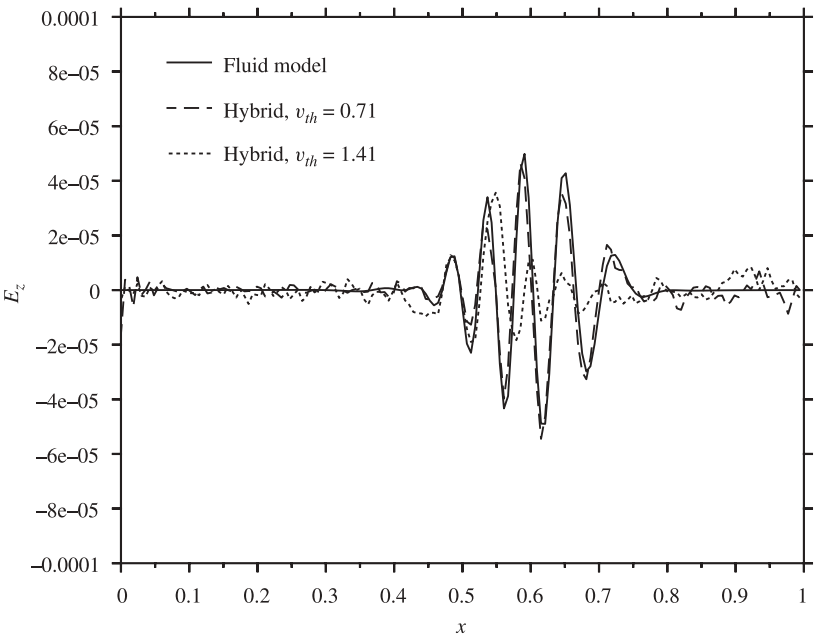

Figure 14. Parallel electric field after the application of the post-simulation spectral filter at $t = 7T_A$. Slice at $z = 7.92$. The fluid model result is unfiltered.

first performing the forward Fourier transform, multiplying the transform by the filtering function and then performing the inverse transform. This is done first in the x-direction and then in the z-direction, but the order of the application is not significant. In the x-direction, 200 grid points were used and so a value of $n = 80$ was chosen. This filters out only the highest of the 100 possible modes as these are the main source of numerical grid scale noise.

In the z-direction, on the other hand, a value of $n = 4$ was used. For any higher value, there was still too much noise to clearly see the signal in the higher-temperature cases. This is not a problem though since the simulation is for the first-order mode $k_z = 2\pi/L_z$ $(i = 2)$ and most of the initial physical information is contained here. Also, although the Landau damping seems to result in some slightly higher-mode structure, the application of this filter to the current does not significantly alter the profile. Therefore, it is safe to assume that applying this filter to the parallel electric field is not leading to a loss of physical information.

The unfiltered fluid parallel electric fields and filtered values for the hybrid code using $v_{th} = 0.71$ and 1.41 (2×10^6 particle simulation) are displayed in Fig. 14. As expected, the parallel electric field in the $v_{th} = 0.71$ case does not diverge significantly from the fluid model, but the damping in the $v_{th} = 1.41$ case is clearly visible. Therefore, even though the field is not visible directly in the simulations, it is behaving as expected and is consistent with the other model variables. The parallel electric field in the $v_{th} = 4.24$ case is not visible even with the filtering, but this can be rectified by increasing the particle number.

Our analysis implies that the electrons are not strongly affected by the high-frequency noise, but are mainly responding to the low-frequency parallel electric field signature. It is believed that the signal-to-noise ratio is so much worse than for

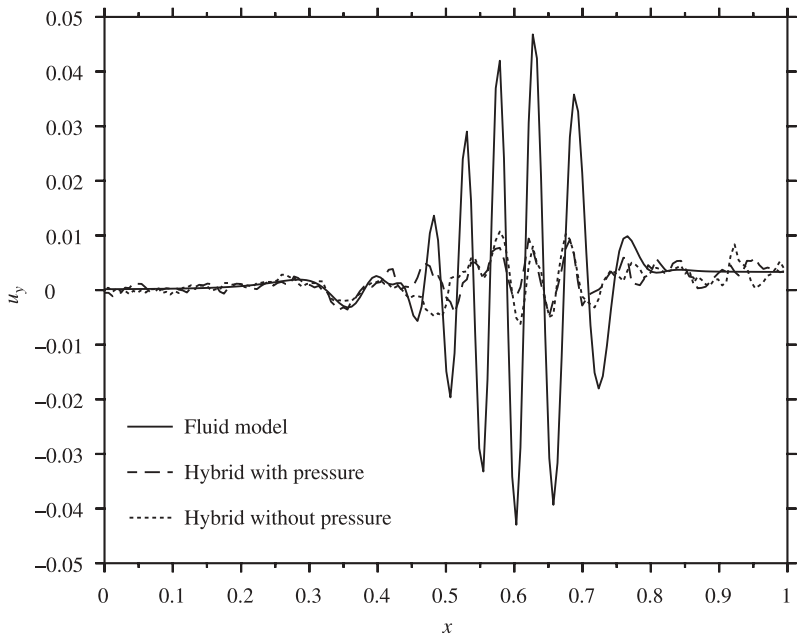

Figure 15. Comparison of azimuthal velocity from the fluid code (solid line) and hybrid code with (dashed line) and without pressure term (dotted line) at $t = 8.0T_A$. For the hybrid simulation $v_{th} = 1.41$ and $n_p = 1 \times 10^6$. Slice at $z = 4$.

all other variables because the determination of E_z involves taking the divergence and then integration of already somewhat noisy quantities (i.e. j_e).

4.7. Significance of the pressure term

Figure 15 illustrates a comparison of the parallel current density from the fluid code (solid line) and the hybrid code with (dashed line) and without the pressure term (dotted line). The negligible difference between the two hybrid model runs illustrates that for the parameters considered here, electric field contributions due to electron pressure are negligible and most of the important physics comes via the electric field generated to enforce quasi-neutrality.

4.8. Damping rate comparison

From the cold plasma equations and the drift kinetic equation (see the appendix), the dispersion relation for a SAW is given by

$$\omega^2 = k_z^2 V_A^2 \left\{ 1 + \frac{i k_x^2}{\omega \mu_0 \frac{-ie^2 n\omega}{k_z^2 k_B T} [1 + \epsilon Z(\epsilon)]} \right\}^{-1}, \tag{4.4}$$

where Z is the plasma dispersion function. This equation can be solved numerically and the damping rate calculated for comparison with the simulation results. Figure 16 illustrates the log of the average value of the current density j_z between $x = 0.5$ and 0.6 (for a slice along $z = 9$) as a function of time between 300 and 800 s ($0.36T_A \leqslant t \leqslant 0.96T_A$). Superimposed is a linear best-fitting line with regression statistics

$$y = (-0.0042 \pm 0.0005)t + 0.5 \pm 0.3 \tag{4.5}$$

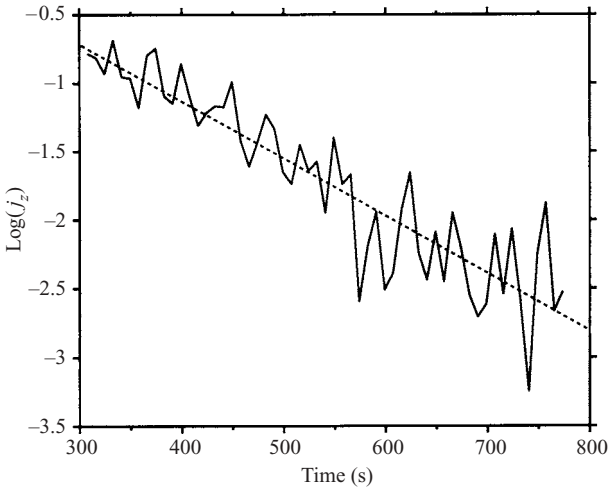

Figure 16. Log of the average absolute value of the parallel current density between $x = 0.5$ and 0.6 versus time for a slice along $z = 7.92$ (solid line) and best-fitting line (dashed line). Data for $t < 300$ s are truncated.

of which the slope gives the damping rate of the resonance $\gamma = -0.0042 \pm 0.0005\ \mathrm{s}^{-1}$. This result can be compared with the values obtained from the imaginary part of the kinetic dispersion relation. This is only a rough comparison as the Alfvén velocity profile changes from 2 to 2.6 in the range considered and the resonance narrows from about $k_x \approx 2\pi/0.1R_E$ to $2\pi/0.05R_E$ as the resonance evolves. Assuming the local Alvén wave speed and electron inertial length at $x = x_r$, damping rates for the $v_{th} = 1.41$ distribution function are calculated to be 0.0016 and 0.0058 s^{-1} for $k_x = 2\pi/0.1R_E$ and $2\pi/0.05R_E$, respectively. Thus the numerical damping rates and that obtained from the kinetic dispersion relation are in the same range.

5. Simulations with conducting boundary conditions

5.1. Modifications to the periodic model

The Earth's ionospheric boundaries are highly conducting and therefore as a first approximation to such boundaries, we modified the code to enforce perfectly conducting boundary conditions at $z = 0$ and L_z. These are $u_x = u_y = b_y = 0$ and $\partial b_x/\partial z = \partial b_z/\partial z = \partial j_z/\partial z = \partial E_z/\partial z = 0$. The radial boundaries are the same as before. The major structural difference between the periodic model and the new model is the addition of two guard cells at each end $z < 0$ and $z > L_z$ to enforce the boundary conditions. The actual boundary points are at the midpoints between the outer two grid cells and the inner grid cells.

The boundaries for the particles are handled by allowing the electrons to freely propagate into the guard cell regions, as if no boundaries existed at $L = 0$ and L_z, responding to the forces imposed on the guard cells by the fluid boundary conditions. The particle moments are then collected at only the grid cells in the region $0 < z < L_z$. The boundary conditions for the current and pressure moments are then imposed on the guard cells as with the case of the fluid. When the electrons reach the last guard cell at either end, they are then reflected back

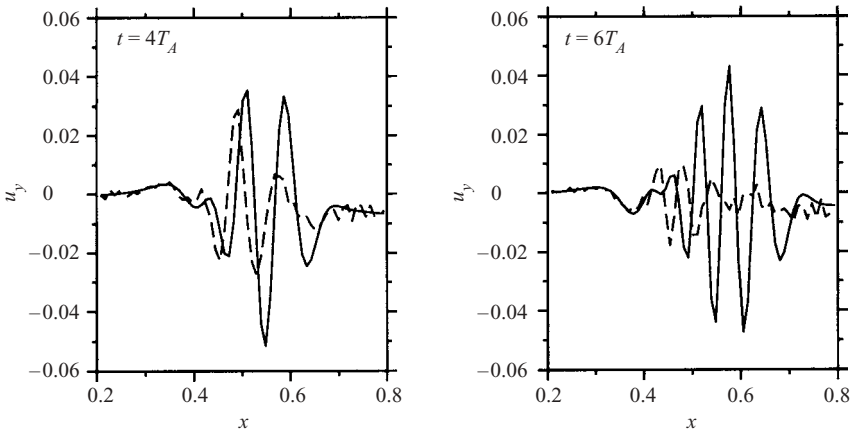

Figure 17. Comparison of the azimuthal velocity from the fluid model (solid line) and the hybrid model with conducting boundary conditions (dashed line) using the $v_{th} = 1.41$ initial electron distribution function for $k_z = \pi/L_z$. Slice at $z = 8.44$.

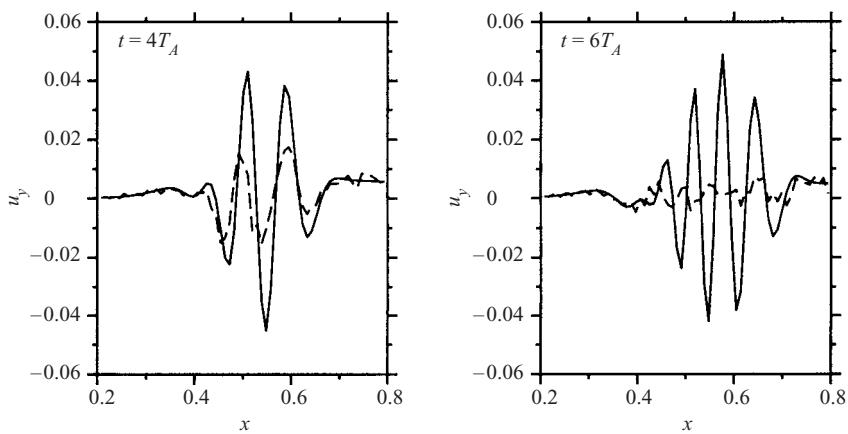

Figure 18. Comparison of azimuthal velocity for the fluid code (solid line) and the hybrid code with conducting boundaries (dashed line) for $v_{th} = 1.41$ and $k_z = 2\pi/L_z$. Slice at $z = 3.94$.

into the box to conserve the particle number. This reflection appears to introduce some relatively large density fluctuations in the guard cell regions, but as long as the initial SAW amplitude and distribution function temperature are maintained in the range considered here, these fluctuations do not affect the results significantly. For much higher temperature and SAW amplitudes a different scheme of handling the perfectly conducting boundary conditions must be derived. For all the simulations presented here the number of radial grid points is $n_x = 128$ and the number of field-aligned grid points is $n_z = 20$.

5.2. Numerical results

In this section, we present two simulations for the $v_{th} = 1.41$ initial Maxwellian distribution function, used in the periodic model, but now we consider the cases of $k_z = \pi/L_z$ and $2\pi/L_z$.

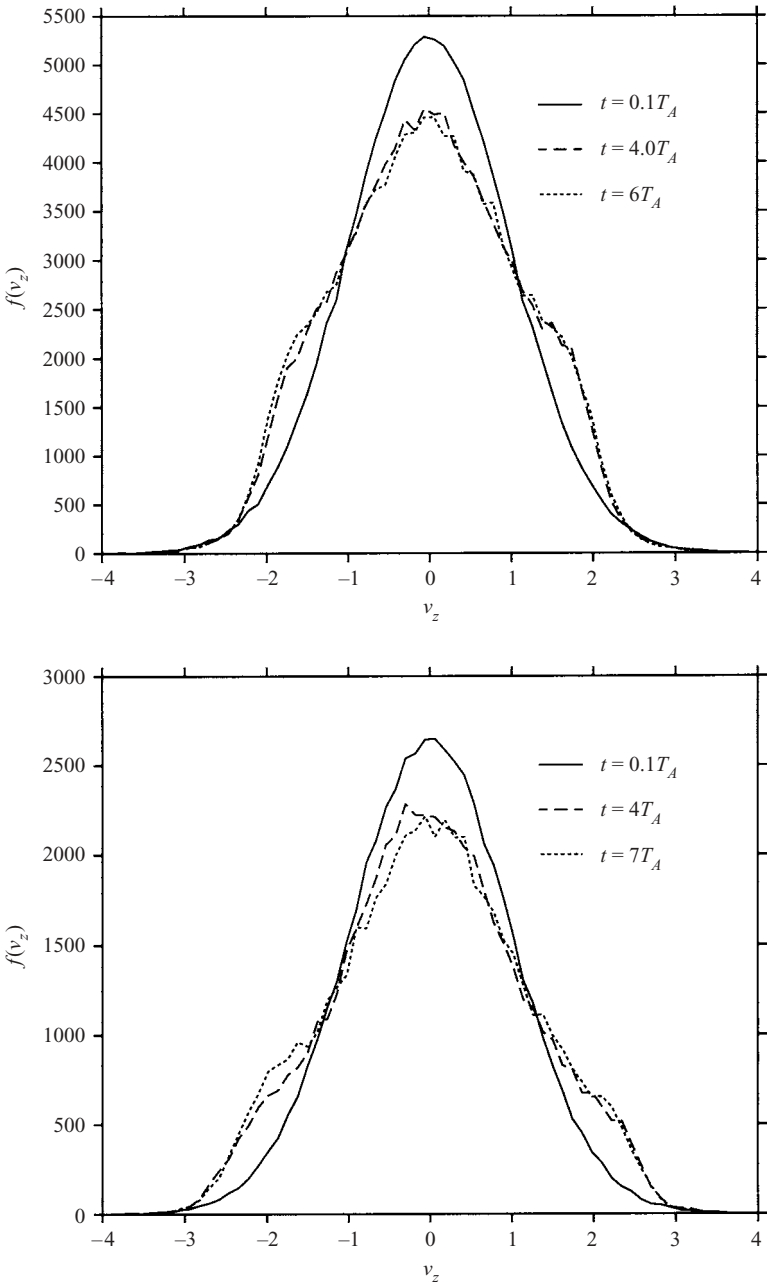

Figure 19. Evolution of distribution function for the hybrid model with conducting boundary conditions for $v_{th} = 1.41$ with $k_z = \pi/L_z$ (top) and $k_z = 2\pi/L_z$ (bottom).

For the fundamental mode, $k_z = \pi/L_z$, the resonance frequency and period are, respectively, half and twice the values for $k_z = 2\pi/L_z$. For both wavenumbers, ten period runs were conducted and so the former case actually evolved for twice as long in physical time. For each simulation, 70 000 time steps were used and Figs 17 and 18 illustrate the evolution of the equatorial azimuthal velocity as a function

of time for $k_z = \pi/L_z$ and $2\pi/L_z$, respectively. In both cases, the damping of the SAW is clearly evident but it is slightly stronger in the first-order mode case. In addition, there is a slightly stronger shift to the right between the hybrid and fluid cases in the fundamental mode simulation relative to the latter. As mentioned previously, this shift is most probably due to the initial propagation of a kinetic SAW in the direction of decreasing Alfvén wave speed. The shift may be more dramatic in the fundamental mode case since the kinetic SAW would have twice as long to propagate relative to the first order mode case.

The evolution of the distribution function in both cases is illustrated in Fig. 19. Both distribution functions are strongly modified due to wave–particle resonance, which is consistent with the decrease in the amplitude of u_y. It should be noted that even though the frequency has different values for the two different wavenumbers, the ratio ω/k_z is the same in both cases. Therefore, it is consistent that the modification of the distribution function should be taking place around $v_z = \pm 2$. The shape is slightly different in both cases, but this may have something to do with how the electrons interact with the different SAW modes. Also, in the first-order mode case, the evolution of the distribution function shows more modification around $v_z = 0$ than in the case with periodic boundary conditions and may be a function of how the boundaries are being handled for the electrons.

These results indicate a qualitative similarity between the results for the first-order mode here and the simulations with periodic boundary conditions. A more quantitative comparison can be made through a comparison of the damping rate. The same procedure as used previously yields a value of $-0.005 \pm 0.001\,\mathrm{s}^{-1}$, which is larger than, but of the same order of magnitude as the damping rate measured for the $k_z = 2\pi/L_z$ case with the periodic model. Therefore, the different boundary conditions do not seem to strongly effect the evolution of the system for the parameters we used.

It should be noted that for this model, the filter described in Sec. 4.6 was not used owing to issues concerning filtration at the perfectly conducting boundaries. However, the temperature considered here is sufficiently small that noise effects were minimal.

6. Conclusions

We have developed a self-consistent hybrid MHD–kinetic box model for studying low-frequency wave–particle interactions in standing SAWs, but the model is applicable to any SAW system as long as the minimum scale length is above the ion gyroradius and $k_\perp \gg k_\parallel$. The model consists of the guiding centre equations for the electron dynamics and the cold plasma equations. The system is closed via an expression for the parallel electric field, including the current density and pressure moments of the electron distribution function.

Simulations were conducted with the model in the limits $v_{th} \ll V_A$, $v_{th} \approx V_A$ and $v_{th} > V_A$. In the first case, the results were found to agree well with the cold plasma MHD results including the formation of an inertial Alfvén wave. In the latter two cases, the SAW was strongly Landau damped. The numerical damping rate was shown to agree well with that predicted by a dispersion relation derived from the drift kinetic equation and the cold plasma MHD equations. Initial formation of a kinetic Alfvén wave that was strongly damped was noted in the higher-temperature cases as well. We have investigated the noise properties of the simulation model

and have shown that the noise does not effect the simulation results and the filtered electric field is consistent with other model variables. The simulations were performed for both perfectly conducting and periodic boundary conditions, but the choice of boundary conditions did not strongly influence the quantitative evolution of the system.

It should be noted that although we have assumed existing standing SAWs in all the simulations, the code is completely general and can also be used to examine the formation of such a system from the mode-conversion process. In addition, the box geometry considered here neglects important physical effects such as the converging magnetic field topology (Rankin et al. 1999) that is fundamental to both FLRs and solar coronal loops. Therefore, we are currently developing this model in dipolar coordinates.

Acknowledgements

This research has been supported in part by the Natural Sciences and Engineering Research Council of Canada. The authors also acknowledge R. Rankin, V. T. Tikhonchuck and I. Voronkov for many useful discussions.

Appendix A. Kinetic dispersion relation

Using the cold plasma equations and defining a dependence of $e^{i(k_x x+k_y y+k_z z)-i\omega t}$, it is straightforward to derive a dispersion relation for the periodic system as

$$\omega^2 = k_z^2 V_A^2 \left(1 + \frac{ik_x^2}{\omega\mu_0\sigma_z}\right)^{-1}, \tag{A 1}$$

where it has been assumed that $k_y = 0$ and an Ohm's law $E_z = j_z/\sigma_z$ has been used to relate the field-aligned electric field and current. In order to determine the field-aligned conductivity σ_z, we start with the general drift kinetic equation (from Baumjohann and Treumann 1996)

$$\frac{\partial f_d}{\partial t} + \nabla_{\mathbf{r}_g} \cdot (\mathbf{v}_d f_d) + \frac{\partial}{\partial v_\parallel}\left(\frac{F_\parallel}{m} f_d\right) = 0, \tag{A 2}$$

where

$$\mathbf{v}_d = \frac{v_\parallel \mathbf{B}}{B} + \mathbf{v}_E + \frac{\mathbf{F}\times\mathbf{B}}{B^2} \tag{A 3}$$

$$\mathbf{v}_E = \frac{\mathbf{E}\times\mathbf{B}}{B^2} \tag{A 4}$$

$$F_\parallel = -\mu\nabla_\parallel B + qE_\parallel \tag{A 5}$$

$$\mathbf{F}_\perp = -\mu\nabla_\perp \mathbf{B} - mv_\parallel^2 \frac{\mathbf{R}_c}{R_c^2} - m\frac{d\mathbf{v}_E}{dt}, \tag{A 6}$$

where $\mathbf{r}_g$ is the guiding centre position, $\mathbf{v}_d$ is the guiding centre velocity and $\mathbf{F}$ is the force applied to the particles. For electrons, the $\mathbf{E}\times\mathbf{B}$ drift is negligible and the low-frequency nature of field line resonances allows us to neglect the polarization drift as well. Therefore, $v_\perp \approx 0$. This, along with the lack of curvature simplifies

the full drift kinetic equation to

$$\frac{\partial f_d}{\partial t} + \frac{\partial}{\partial z}(v_z f_d) - \frac{\partial}{\partial v_z}\left(\frac{eE_z}{m_e} f_d\right) = 0, \tag{A 7}$$

where we have replaced the '$\|$' notation with z and $q = -e$. Linearizing such that $f_d = f_0 + f_1$, where f_0 and f_1 are the equilibrium and perturbed distributions, respectively, and keeping only first-order terms, the kinetic dispersion relation becomes

$$\frac{\partial f_1}{\partial t} + v_z \frac{\partial f_1}{\partial z} - \frac{eE_z}{m_e}\frac{\partial f_0}{\partial v_z} = 0, \tag{A 8}$$

where the fact that v_z and z are independent variables has also been used. This kinetic equation is the same as that has been used for low-frequency phenomena by Tikhonchuk and Rankin (2000) and Antonsen and Lane (1980). Assuming the dependence $e^{ik_z z - i\omega t}$, the electron kinetic equation can be solved for the perturbed distribution

$$f_1 = \frac{-ieE_z \frac{\partial f_0}{\partial v_z}}{k_z m(v_z - \omega/k_z)}. \tag{A 9}$$

The current is related to this perturbed distribution via

$$j_z = -e \int d^3v\, v_z f_1.$$

Performing the integration using a Maxwellian distribution for f_0

$$f_0 = n\left(\frac{m}{2\pi k_B T}\right)^{1/2} e^{-mv_z^2/2k_B T}\delta(v_x)\delta(v_y) \tag{A 10}$$

yields the following expression relating the field-aligned current and electric field:

$$j_z = \frac{-ie^2 n\omega}{k_z^2 k_B T}[1 + \epsilon Z(\epsilon)]E_z, \tag{A 11}$$

where $\epsilon = \frac{\omega}{k_z}\sqrt{\frac{m}{2k_B T}}$ and Z is the plasma dispersion function defined by

$$Z(\epsilon) = \frac{1}{\sqrt{\pi}}\int_{-\infty}^{\infty} \frac{dx\, e^{-x^2}}{x - \epsilon}. \tag{A 12}$$

Comparing (A 11) with Ohm's law, $J_z = \sigma_z E_z$, the corresponding expression for the field-aligned conductivity is given by

$$\sigma_z = \frac{-ie^2 n\omega}{k_z^2 k_B T}[1 + \epsilon Z(\epsilon)] \tag{A 13}$$

and substituting this into expression (A 1) the complete kinetic dispersion relation is then

$$\omega^2 = k_z^2 V_A^2 \left\{1 + \frac{ik_x^2}{\omega\mu_0 \frac{-ie^2 n\omega}{k_z^2 k_B T}[1 + \epsilon Z(\epsilon)]}\right\}^{-1}. \tag{A 14}$$

In the cold plasma limit (when $V_A \gg V_{th}$), the plasma dispersion function can be expanded as

$$Z(\epsilon) = -\frac{1}{\epsilon} - \frac{1}{2\epsilon^2} - \frac{1}{4\epsilon^3} \tag{A 15}$$

and using this (with the first two terms) in the kinetic dispersion relation allows the simplification of the dispersion relation to that of the inertial Alfvén wave as would be expected,

$$\omega^2 = \frac{k_z^2 V_A}{1 + k_x^2 \lambda_e^2}. \tag{A 16}$$

In the warm plasma limit ($V_A \ll v_{th}$), the asymptotic expansion of the plasma dispersion function is given by

$$Z(\epsilon) = -2\epsilon\big(1 - \tfrac{2}{3}\epsilon^2\big) \tag{A 17}$$

and the conductivity becomes

$$\sigma_z = \frac{-ie^2 n\omega}{k_z^2 k_B T}\big(1 - 2\epsilon^2 + \tfrac{4}{3}\epsilon^3\big). \tag{A 18}$$

Since $\epsilon^2 \ll 1$, the conductivity can be simplified to

$$\sigma_z = \frac{-ie^2 n\omega}{k_z^2 k_B T} \tag{A 19}$$

and the dispersion relation becomes

$$\omega^2 = k_z^2 V_A^2\big(1 + \tfrac{1}{2}k_x^2 \rho_s^2\big), \tag{A 20}$$

where $\rho_s = \lambda_e v_{th}/V_A$. This warm electron dispersion relation generally appears with an additional term owing to ion gyroradius effects (see Lysak and Lotko 1996). The absence of the term here emphasizes that for the model to be valid, the minimum scale lengths should be above the typical ion gyroradii.

As an aside, it is fairly straightforward to illustrate the derivation of the simplified generalized Ohm's law. Starting with the simplified drift kinetic equation,

$$\left(\frac{\partial}{\partial t} + v_z \frac{\partial}{\partial z}\right) f_1 = \frac{eE_z}{m_e}\frac{\partial f_0}{\partial v_z}$$

and assuming v_z is not a function of t and z, integration over velocity yields

$$\frac{\partial j}{\partial t} - e\frac{\partial}{\partial z}\int_{-\infty}^{\infty} dv_z\, v_z^2 f_0 = \frac{e^2 n_e}{m_e} E_z,$$

where $n_e = \int_{-\infty}^{\infty} dv_z\, f_0$ and $j = -e\int_{-\infty}^{\infty} dv_z\, v_z f_1$. As there is no bulk fluid flow in the z-direction, the electron pressure is given by

$$P_e = m_e \int_{-\infty}^{\infty} dv_z\, v_z^2 f_0$$

and therefore we have

$$\frac{\partial j}{\partial t} - \frac{e}{m_e}\frac{\partial}{\partial z} P_e = \frac{e^2 n_e}{m_e} E_z.$$

Rearranging and using the definition for electron inertial length $\lambda_e = m_e/(\mu_0 n_e e^2)$ yields

$$E_z = \mu_0 \lambda_e^2 \frac{\partial j_z}{\partial t} - \frac{1}{n_e e}\frac{\partial P_e}{\partial z}.$$

References

Antonsen, T. M. and Lane, B. 1980 Kinetic calculations for low frequency instabilities in inhomogeneous plasmas. *Phys. Fluids* **23**, 1205–1214.

Baumjohann, W. and Treumann, R. A. 1996 *Basic Space Plasma Physics*. London: Imperial College Press.

Beliën, A. J. C., Martens, P. C. H. and Keppens, R. 1999 Coronal heating by resonant absorption: the effect of chromospheric coupling. *Astrophys. J.* **526**, 478–493.

Birdsall, C. K. and Langdon, A. B. 1991 *Plasma Physics via Computer Simulation*. Bristol: Hilger.

Busnardo-Neto, J., Pritchet, P. L., Lin, A. T. and Dawson J. M. 1977 A self-consistent magnetostatic particle code for numerical simulation of plasmas. *J. Comput. Phys.* **23**, 300–312.

Fenrich, F. 1997 Field line resonance: observation and theory, *PhD thesis*, University of Alberta.

Gould, H. and Tobochnik, J. 1996 *An Introduction to Computer Simulation methods*. Reading, MA: Addison-Wesley.

Hui, C.-H. and Seyler, C. E. 1992 Electron acceleration by Alfvén waves in the magnetosphere. *J. Geophys. Res.* **97**, 3953–3963.

Ionson, J. A. 1978 Resonant absorption of Alfvénic surface waves and the heating of the solar coronal loops. *Astrophys. J.* **226**, 650–673.

Lysak, R. L. and Lotko, W. 1996 On the kinetic dispersion relation for shear Alfvén waves. *J. Geophys. Res.* **101** 5085–5094.

Lyster, P. M. and Leboeuf, J.-N. 1992 A fluid-ion and particle–electron model for low-frequency plasma instabilities. *J. Comput. Phys.* **102**, 180–193.

Okuda, H., Lee, W. W. and Cheng, C. Z. 1979 Electrostatic and magnetostatic particle simulation models in three dimensions. *Comp. Phys. Commun.* **17**, 233.

Parks, G. K. 1991 *Physics of Space Plasmas*. Reading, MA: Addison-Wesley.

Rankin, R., Samson, J. C. and Tikhonchuk, V. T. 1999 Parallel electric fields in dispersive shear Alfvén waves in the dipolar magnetosphere. *Geophys. Res. Lett.* **26**, 3601–3604.

Streltsov, A. V. and Lotko, W. 1999 Small-scale, 'electrostatic' auroral structures and Alfvén waves. *J. Geophys. Res.* **104**, 4411–4426.

Tikhonchuk, V. T. and Rankin, R. 2000 Electron kinetic effects in standing shear Alfvén waves in the dipolar magnetosphere. *Phys. Plasmas* **7**, 2630–2645.

Winske, D. and Quest, K. B. 1986 Electromagnetic ion beam instabilities: comparison of one- and two-dimensional simulations. *J. Geophys. Res.* **91**, 8789–8797.